Microelectronic Engineering 287 (2024) 112154

Contents lists available at ScienceDirect

Microelectronic Engineering

journal homepage: www.elsevier.com/locate/mee

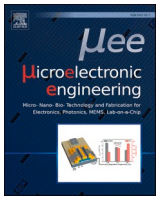

Silicon microresonator arrays: A comprehensive study on fabrication techniques and pH-controlled stress-induced variations in cantilever stiffness

G. Brunetti [a,b,c,1], A. De Pastina [d,1], C. Rotella [c], V. Usov [c], G. Villanueva [e], M. Hegner [c,*]

[a] Tissue Engineering Research Group (TERG), Department of Anatomy & Regenerative Medicine, Royal College of Surgeons in Ireland (RCSI), Dublin, Ireland
[b] Advanced Materials and Bioengineering Research (AMBER) Centre, Trinity College Dublin (TCD), Dublin, Ireland
[c] Center for Research on Adaptive Nanostructures and Nanodevices (CRANN), School of Physics, Trinity College Dublin (TCD), Dublin, Ireland
[d] Silicon Austria Labs, Microsystem Technologies, Villach, Austria
[e] Advanced NEMS Laboratory, École Polytechnique Fédérale de Lausanne (EPFL), Switzerland

ARTICLE INFO

Keywords:
Silicon microcantilevers
Cantilever arrays
Microfabrication
Micromechanical sensors
pH-relative liquid environment
Sensor stiffness

ABSTRACT

We introduce a detailed design and fabrication process of Silicon microcantilever arrays for biomolecular detection in liquid environment, utilized with laser readout. We present typical fabrication problems and provide related solutions to obtain high quality resonators via a robust, reproducible and high-yield process. Sensors in these arrays are individually functionalized with self-assembled chemical monolayers exposing various pH-active end-groups into solution. Dynamic-mode controlled frequency measurements in varying pH solutions result in stress-induced change of the sensor spring constant. pH changes in the solution lead to deprotonation of exposed functional chemical groups at high pH and the repulsive charges induced strain is proportional to the quantity and confinement of charges at the sensor interface. These built-up strains that affect the mechanical stiffness can be reversibly relaxed when exposed again to low pH environments.

1. Introduction

Microcantilevers have been employed in a variety of sensing applications in the past decades, being able to produce a fast and reliable response to changes of mass, temperature, and surface stress. Detection of microscale forces and surface topography via atomic force microscopy [1], biomolecular detection [2–8], single cell analysis when integrated with microfluidic channels [9,10] and integrated transduction [11], pressure sensing [12], or calorimetry [13,14], are just a few among a wide range of applications reported in literature [15,16].

The microfabrication process of microcantilevers varies in number of steps and complexity, based on (i) the chosen structural material, typically silicon or polymer depending on the application, and (ii) the planned detection technique (e.g., external optical readout or integrated electrodes on chip). Even though the process steps involved are typically standard, it is no trivial to obtain flat-released structures with well controlled dimensions and polished residue-free surfaces, especially when complex geometries such as array configuration or backside combs are involved [17]. However, the microfabrication details and fine tuning, and the typical issues that can be encountered during the process are normally not found in the literature.

Hence, objectives of these manuscript are to (i) discuss in detail the fabrication process of Silicon microcantilever arrays, (ii) highlight the material choices and process steps, (iii) present typical problems and related solutions to obtain high quality resonators via robust, reproducible and high-yield process and (iv) test this novel configuration of Silicon cantilever arrays throughout the analysis of the study of their spring constant within pH-based frequency measurements. Main outcome is a novel and optimized 3-mask fabrication procedure that leads to a yield larger than 90%. Moreover, this process has a wide range of applications. It is not limited to only cantilevers, but also to other types or resonant structures such as doubly clamped beams or membranes.

* Corresponding author.
E-mail address: hegnerm@tcd.ie (M. Hegner).
[1] Contributed equally.

https://doi.org/10.1016/j.mee.2024.112154
Received 18 December 2023; Received in revised form 29 January 2024; Accepted 3 February 2024
Available online 5 February 2024

2. Design

We focus on microcantilever arrays for biomolecular detection in liquid environment, designed for optical readout and requiring surface functionalization prior to the immersion in the fluid sample. Such devices need an ultra-clean and smooth surface to allow for focusing and reflection of an optical laser, which must go through the top glass of a custom-made microfluidic chamber. Details about experimental setup and microfluidic measurement chamber can be found in previously published works [17,18]. Indeed, a laser spot below 10 μm of radius is necessary to ensure the simultaneous detection of multiple out-of-plane resonance modes, and to limit the crosstalk with the adjacent cantilevers (typical pitches are 170 μm, gap between two adjacent sensors 100 μm).

In addition, the cantilevers are designed with a specific geometry to allow for molecule immobilization via capillary method functionalization [17,19]: this allows to incubate each cantilever of the array in a dedicated liquid solution to later tackle different biorecognition events within the same experiment.

Fabricated cantilevers (Cls) are 400 μm long and 70 μm wide, with a thickness set in a range between 0.5 μm and 3 μm, uniformly defined via a dedicated etching step. These dimensions were reduced with respect to the previous benchmarking microchip devices (500 μm × 100 μm × 1 μm, pitches were at 250 μm), to fit a higher number of resonators per chip, while maintaining the original chip body dimensions (3 mm in width) compatible with the experimental interface [17,18]. This new configuration enables placing 18 cantilevers per chip, compared to the 8-cantilever configuration of the previous generation of devices. Such a high number of sensors represents a crucial step ahead if compared with similar devices used previously. This novel design provides more versatility in functionalization and allows for increased averaging of identically sensitized sensors, thus improving statistical robustness and experimental efficiency [4].

The wafer-level fabrication is based on a 3-mask design, shown in Fig. 1 for a single chip.

The first mask (yellow box, in Fig. 1), consisting of a rectangular aperture to be defined via photolithography and wet KOH etching, sets the resonator thickness and the mechanical clamp (hinge region). Precise hinge definition is particularly important when the devices are operated in static mode, which requires the exact knowledge of the cantilevers length to extract the stress value from measured deflection. Without this mask, the length of the resonators would otherwise vary among adjacent sensors due to the isotropic release at the end of the fabrication process, making it difficult to average and compare the responses of several devices within the array. The second mask (purple, in Fig. 1) patterns the cantilever geometry, the 3 mm-wide chip body, 80 μm-wide cleavage lines. The third and final mask (black grid, in Fig. 1) defines the backside comb, fundamental during the functionalization stage: before experiment, the microresonator array is aligned and incubated into an array of glass microcapillaries containing the respective functionalization solutions. The backside comb prevents the microcapillaries from reaching the chip body, which would offer a cross contamination path between adjacent resonators.

Each wafer contains 308 chips, which can be easily detached manually with the help of tweezers, thanks to the cleavage lines defined in masks 2 and 3.

In order to select a cantilever width compatible with the lateral resolution of the existing optical setup [17], prior to the wafer-scale fabrication, arrays of narrower cantilevers of different dimensions were produced. Chips from the previous design and fabrication run were processed by splitting wider cantilevers via focused ion beam milling, or via partial masking of wider cantilevers with Ga ions implantation followed by dry etching of unmasked cantilever areas. The narrower cantilevers were tested for their functionality and compatibility with the setup, resulting in the selection of the new dimensions for the following wafer-scale fabrication run. The optimal selected dimensions are 400 μm-long and 70 μm-wide cantilevers. The thickness spans a range between 0.5 μm and 3 μm, compatible with the excitation of higher resonant flexural modes and with the frequency range of the custom-made piezo actuator.

3. Fabrication

The microfabrication is carried out on a 7–2-500 Silicon-On-Insulator (SOI) substrate, 100 mm in diameter. Fig. 2 shows the

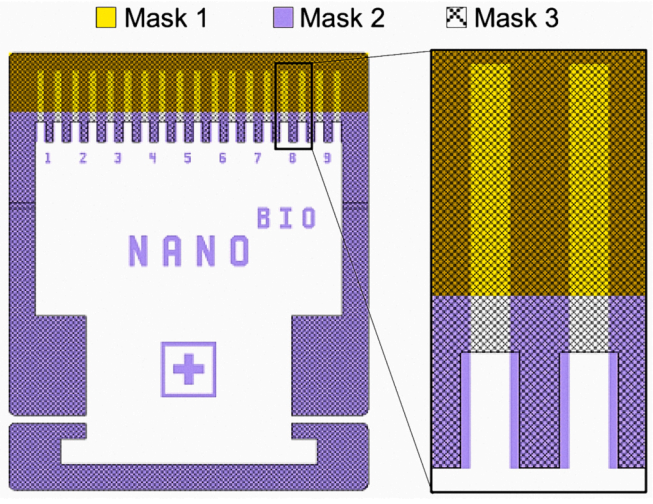

Fig. 1. Mask design of an 18-microcantilever chip. The 3-mask fabrication process consists in a first rectangular slot definition (mask 1, yellow), which determines the cantilevers hinge region, thus setting their exact length; the cantilever geometry is patterned via the second photolithographic mask (mask 2, purple); follows the patterning of the backside comb and chip body (mask 3, black grid). The inset shows a zoom-in on two adjacent microcantilevers of the array, of 400 μm × 70 μm dimensions, with a thickness set in a range between 0.5 μm and 3 μm. (For interpretation of the references to colour in this figure legend, the reader is referred to the web version of this article.)

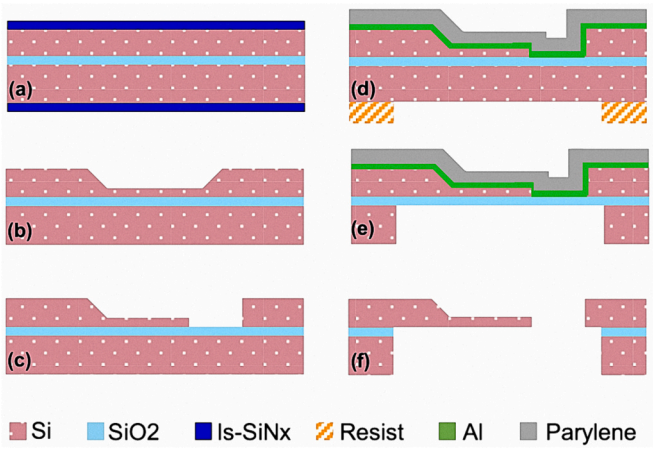

Fig. 2. Microcantilever fabrication process in cross section. (a) The fabrication starts with LPCVD deposition of ls-SiNx on both sides of an SOI wafer. (b) The cantilevers hinge is defined via KOH etching, and is followed by wet etching of ls-SiNx. (c) Resonators geometry is patterned via photolithography and dry etching. (d) Aluminum and parylene C are deposited via sputtering and CVD, respectively, to protect the cantilevers top surface during the subsequent backside processing. (e) A third photolithography defines chip body and backside comb. The buried oxide acts as a stop layer for the wafer-through dry etch. (f) The resonators are finally released by removing the protective Al and Parylene via wet etching and oxygen plasma, respectively, followed by buried oxide wet etching. Dimensions not to scale.

schematic of the fabrication process flow, considering a cross section along the length of one cantilever in the array.

The process starts with low-pressure-chemical-vapor deposition (LPCVD) of 200 nm low stress silicon nitride (Fig. 2(a)). The ls-SiNx on the wafer front side is patterned with the first mask via standard photolithography and C_2F_6-based dry etching, to act as a hard mask during the silicon etch in 40% KOH solution at 50 °C. Fig. 3 shows the optimization of the KOH etching step.

Of utterly importance is the preparation of the silicon surface before the KOH etching step: it is fundamental to remove the native oxide layer on the silicon, which would prevent the uniform etching in KOH and result in uneven etched surface and pyramidal irregularities on the cantilevers surface, as shown in Fig. 3 (e). The native oxide removal on silicon can be performed via 30 s wafer immersion in HF 49%, followed by thorough rinse in DI water, and direct immersion in KOH solution, avoiding drying the wafer.

Accurate calibration of the silicon etching rate in KOH solution is needed to remove the exact silicon amount from the 7 μm–thick device layer, hence defining the cantilevers thickness. The rates were calibrated

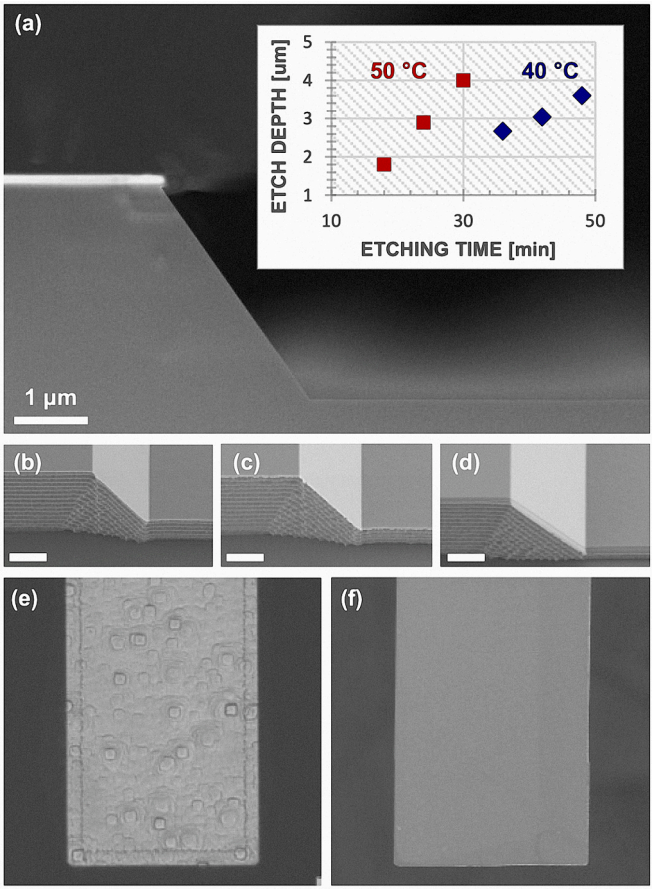

Fig. 3. Optimization of KOH etching for hinge definition. (a) Etching rates were established by taking SEM images of the cross sections of several Si test samples, etched via 40% KOH. Etching rates of 4.2 μm/min and 7.1 μm/min were calculated for KOH 40% at 40 °C (inset, blue diamonds) and 50 °C (inset, red squares), respectively. Calibrating the KOH etching duration allows to set different cantilevers thicknesses on different wafers. The accuracy of a profilometer measuring the etch depth is several 10s nm (the measurement error lies within the symbols shown). In (b-d), tilted SEM images of (b) 2.5 μm-, (c) 2 μm- and (d) 1 μm-thick Si cantilevers are shown, before release. (e) and (f) show the SEM image of the top surface of Si cantilevers (width of sensor 70 μm). It is fundamental to remove the native oxide on the silicon surface right before immersing the wafers in KOH to obtain a smooth etched surface (f) and avoid typical pyramidal defects (e). (For interpretation of the references to colour in this figure legend, the reader is referred to the web version of this article.)

on a sacrificial SOI wafer, patterned, and cleaved into chips, immersed in KOH solutions at different temperatures and for various times. Etching rates of 4.2 μm /hour and 7.1 μm /hour were measured by scanning electron microscope (SEM) imaging of the chips cross sections, for KOH 40% at 40 °C and 50 °C, respectively. The glass beakers containing the heated KOH solutions were placed on a hotplate, the solutions were covered with glass lids to prevent water evaporation and mixed with a magnetic stirrer throughout the process to allow recirculation. Increasing the process temperature is known to accelerate the silicon etching rate, but also to increase the surface roughness of the resulting silicon etched area [20], which would have been incompatible with the requirements set by the optical readout needs of this work. However, no visible difference was observed for the two temperatures considered, therefore the process at 50 °C was selected and the etching time was adjusted when targeting different cantilever thickness, as shown in Fig. 3 (b-d). After silicon etching, follows a 2 h potassium neutralization step HCl 37%. The ls-SiNx is then removed via wet process in HF49% at room temperature for about 70 min (Fig. 2 (b)).

The cantilevers geometry is defined through Mask 2 and patterned via photolithography and Bosch process silicon anisotropic etching (Fig. 2 (c)). Subsequently, a protective layer is deposited on the wafer front (Fig. 2 (d)) to prevent the top surface damaging during the backside pattering. The third mask defines the backside comb and release window, patterned via photolithography and wafer-through dry etching via Bosch process (Fig. 2 (e)). The cantilevers are finally released via buried oxide removal in HF 49% at room temperature, and top protection strip. It must be noted that the buried oxide layer is highly stressed, therefore it should be removed before the protective layer to avoid the cantilevers curling and breaking.

The choice of the front side protective material is crucial and determines the survival of the cantilevers at the end of fabrication process. Two candidates were tested during the process optimization: 2 μm evaporated aluminum and 5 μm CVD parylene C, as shown in Fig. 4.

Thin films evaporation is a non-conformal process [21], therefore the aluminum coverage on the sidewalls of the cantilevers is non optimal. In addition, we noticed that the aluminum film tends to crack during the wafer-through etch step. The combination of the two effects causes the SF6 gas, during the backside Bosch process, to reach the wafer front thus damaging cantilevers sidewalls, resulting in irregular-shape released sensors, as shown in Fig. 4(b). Aluminum can be easily removed via wet etching step, immersing the wafers in Alu etch commercial solution (Microchemicals GmbH) at 35 °C for a few minutes, with an approximate etch rate of 17 μm /min,

On the other hand, Parylene C is deposited via CVD process, and ensures a very conformal coverage of the wafer front. In addition, no cracks are observed during the backside release, resulting in smooth wafer-through etch and perfectly intact cantilevers. However, Parylene C removal results quite challenging: despite several and extensive cycles of oxygen plasma etch, it is still possible to observe residues on the silicon surface of the sensors (Fig. 4(d)). Several organic removers were tested in order to get rid of such residues, the only beneficial treatment resulted from immersing the wafer in Technistrip P1316 high performant remover (Microchemicals GmbH), heating and maintaining the bath at 80 °C for 2 h, and subsequently switching off the hot plate to cool down overnight. However, the surface of the cantilevers was still not fully cleared from the parylene C filaments and patches, which were still observable via SEM imaging.

Given the biosensing application and the need for surface functionalization of the devices fabricated in this work, such result was not acceptable, therefore we opted for a combination of the two strategies to benefit from both materials: the designated front side protection consists in a first layer of 1 μm evaporated aluminum, easy to remove and residue-free on the silicon, followed by 5 μm CVD Parylene C, which ensures conformal and robust protection of the wafer top surface. The protective bilayer is removed, after buried oxide strip in HF 49% for 30 s, via 20 min oxygen plasma, followed by about 5 min in Alu etch

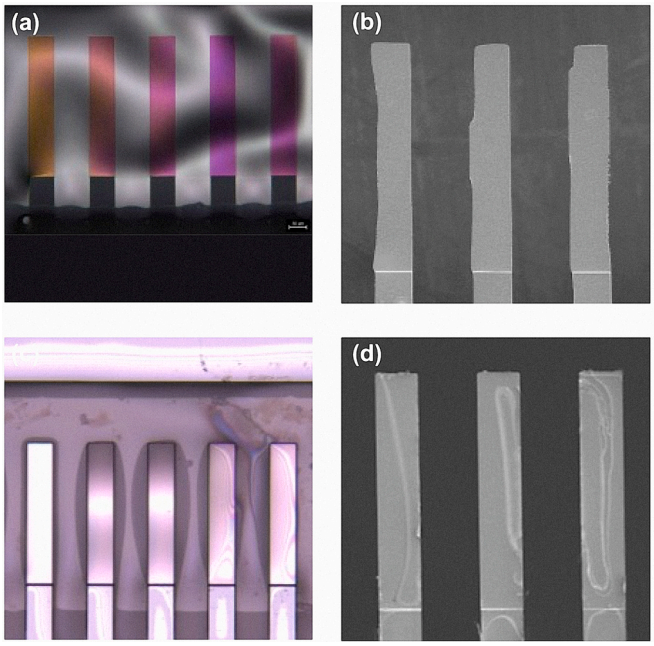

Fig. 4. Aluminum (a, b) versus Parylene C (c, d) protective mask. (a) Optical image of a wafer backside after complete wafer-through dry etch landed on buried oxide. The oxide compressive stress causes wrinkles and cracks in the evaporated aluminum layer, allowing the SF_6 etching gas to access the unprotected resonator side surface. (b) SEM image of cantilevers after full release, with visible cantilever damage, when the Al protective layer is used. (c) Optical image of the cantilever top side after wafer-through dry etch, in case of Parylene protective layer. The conformality of the Parylene film allows to effectively protect the resonators, yielding to successful release without damage (c). However, parylene residues are left on the surface of the cantilevers despite extensive oxygen plasma process, as visible via SEM image (d). (Sensor length 400 μm, widths are 70 μm).

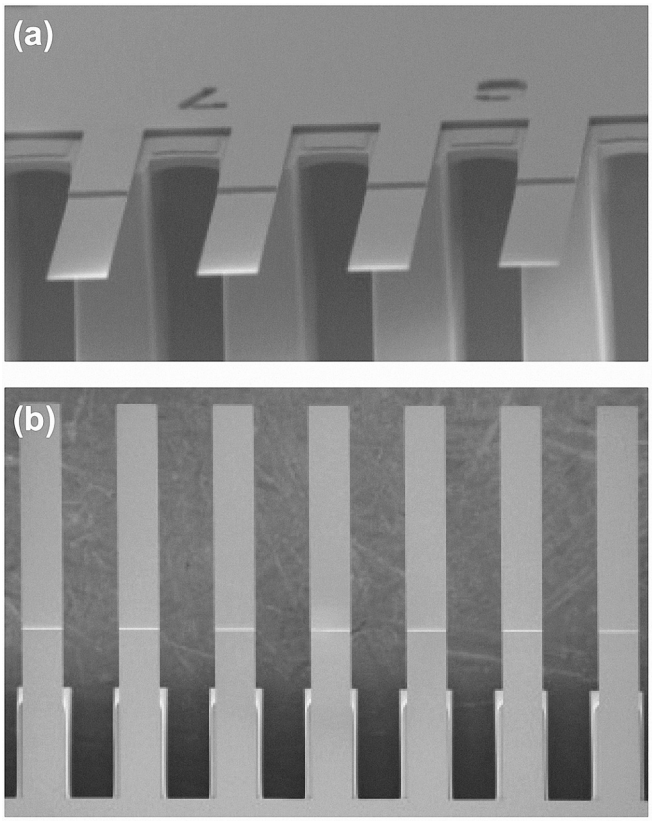

Fig. 5. SEM image of successfully microfabricated silicon microcantilever array. (a) tilted view, which allows to see hinge and backside comb; (b) top view (Sensor length 400 μm, widths are 70 μm, thickness 2.3 μm, pitch 170 μm).

solution.

As a final step, the chips are carefully rinsed in DI water, and directly immersed from static water bath to isopropyl alcohol (IPA) bath, which constitutes the last wet step to avoid stiction and cantilever rupture. The wafer is left to dry in the closed wet bench under gentle laminar flow. The optimization of the full process led to successful microfabrication of silicon microcantilever arrays, with a wafer yield larger than 90%. Fig. 5 shows images of fabricated cantilever arrays.

4. Array validation by the analysis of the sensitivity of the sensors on their micromechanical properties in variable pH-based frequency measurements

As mentioned before, focus of this novel design is an increased output in terms of versatility in functionalization and increased averaging potential thus improving statistical robustness and experimental efficiency. In order to test these newly developed cantilever arrays in a variable liquid environment, a series of experiments are performed on our home-built integrated cantilever array sensor platforms. Mechanical signals are detected via an optical laser beam deflection readout, able to detect cantilever oscillation with mHz − and sub-nanometer resolution. A proportional–integral–derivative controlled phase-locked loop feedback system is directly interfaced with the experimental hardware and able to track up to 4 oscillation modes of 18 sensors in parallel over several hours [17,18].

Building on the deep knowledge of the Hegner lab in the field of biosensing and self-assembled monolayers (SAMs) with microfabricated structures, the goal of the experiments was to investigate the effect of different pH levels of the surrounding environment on the mechanical properties of the cantilevers (frequency, spring constant and mass).

Each cantilever used in the present study is coated with 3 nm of Titanium (deposition rate 0.2 Å/s) and 23/33 nm Gold (top and bottom side, respectively, deposition rate 0.5 Å/s) via e-beam metal evaporation (Temescal FC-2000, Scotech). The top and bottom gold deposition is coating 98% of the surface of the sensor. The side walls and the front face respesent less that 2% of the 3D structure The exposed gold layer allows (i) to optimize the optical detection by maximizing the reflectivity of each cantilever surface and (ii) offers an anchoring platform for the thiol groups of the functionalization molecules. To this end, four chemically different SAMs (Fig. 6 panel B) are utilized to functionalize the 18 sensors individually via capillary cantilever funtionalization as described in detail in [17]. Common to all SAMs are the thiol end-group that covalently interacts with the gold surface. The hydrophobic middle section is chosen with a length of aliphatic CH_2 goups that ensure close packing of the monolayer on the underlying surface [22]. We chose four different chemical endgroups (SAM−COOH, −OH, −CH3, −NH2), 11-Mercaptoundecanoic acid, 11-Hydroxy-1-undecanethiol, 1-undecanethiol and 11-Amino-1-undecanethiol respectively that expose a carboxylic acid, a hydroxyl-, a methyl- and a primary amine- and a methyl-group to the liquid environment surrounding each cantilever (relative pKa reported in Fig. 6, panel (b). Detailed description of the chemicals and cantilever cleaning and coating steps can be found in [6].

The functionalized cantilever array is incubated in three different solutions that represent pH values of 2.5, 7 and 11, respectively (10 mM Citric acid, 10 mM Hepes buffer and 4 mM NaOH). During the whole experiment, a concentration of 1 mM NaCl allows to maintain a proper ionic strength among the three solutions. The native silicon oxide silanol groups can deprotonate at pH >8.5 [23,24]. The fluid chamber volume where the array is mounted is ~6 ul. The analytical platform is

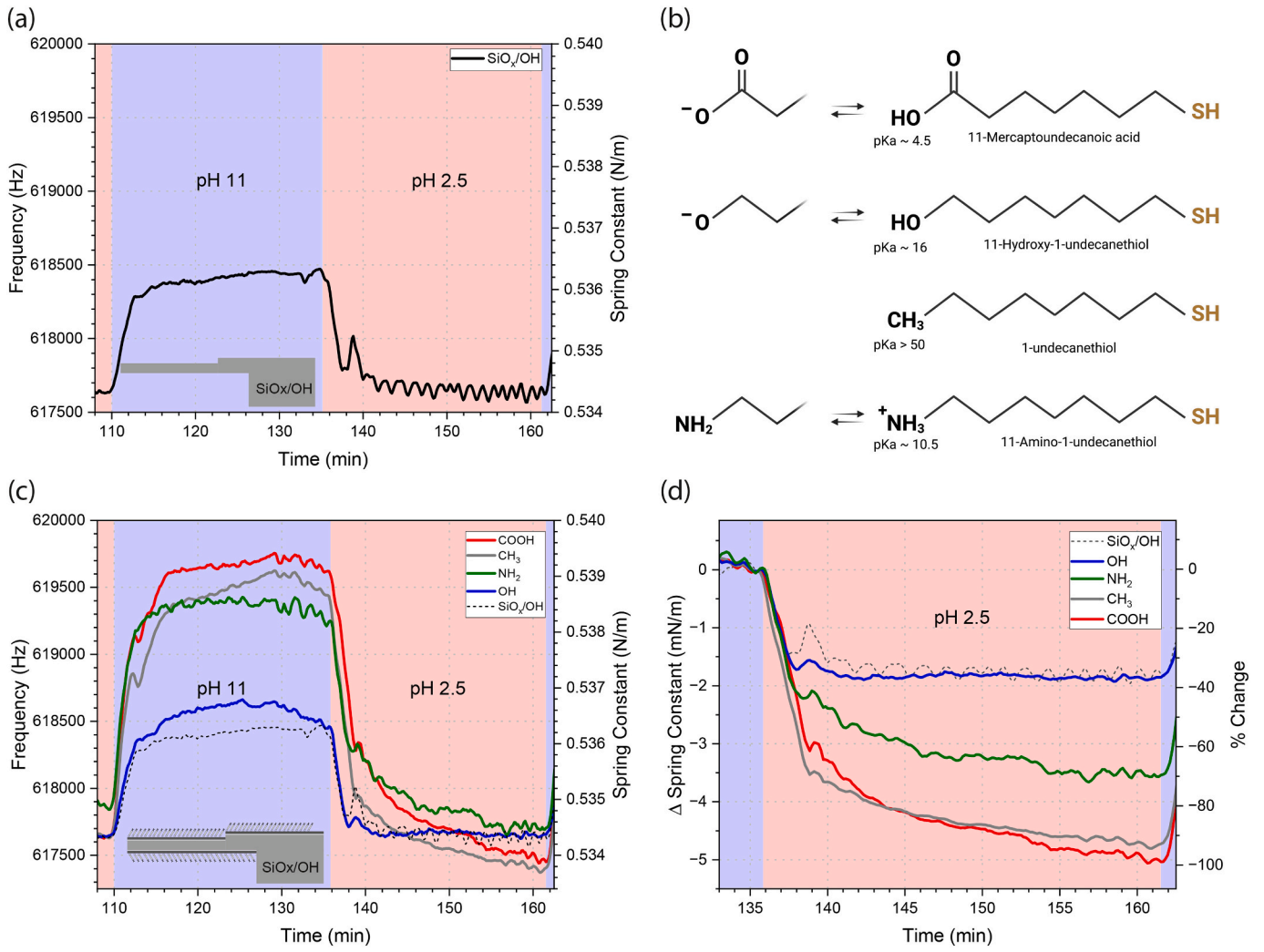

Fig. 6. Cantilever array responses to pH changes. (a) Blank silicon sensor array that does not have any coating exposed to pH 11 and pH 2.5 conditions. The oscillation frequency increases during high pH exposure. Since no molecular mass addition takes place, the indicated change is attributed to changes in sensor surface strain, indicated by a change in spring constant. The line shown represents an average of $n = 12$ sensors. The inset shows a blank silicon sensor. (b) Chemical surface modification of the individual cantilever sensors. The hetero bi-functional alkyl-thiols form self-assembled monolayers (SAMs) on the Ti/Au coated cantilever structures. Four chemicals were chosen to form SAM-COOH, SAM-OH, SAM-CH_3 and SAM-NH_2 interfaces. The pK_a of the solution exposed functional group is indicated. (c) SAM functionalized sensors incubated in alternated pH 2.5 – pH 11 – pH 2.5 solutions. SAM-COOH ($n = 6$, red), SAM-NH_2 ($n = 4$, green), SAM-OH (n = 4, blue), SAM-CH_3 (n = 4, grey), SiO_x/OH (from Figure (a) as underlying graph, black dashed). At $t = 110$ min the pH is switched from pH 2.5 to 11 and sensor frequency is changing to a higher frequency. After switching back to pH 2.5 at 136 min sensor frequencies recover to a lower value. The inset shows a silicon sensor coated with Ti/Au and hetero-bifunctional self-assembled monolayers (not drawn to scale). (d) Sensors at pH 11 under strain due to charging (strain normalized to the highest strain in the COO^- sensors). Switching back to pH 2.5 at 136 min allows sensors to relax to a lower value. The spring constant in the COO^- is relaxing by ~5 mN/m. The relative percentage of softening depends on the built-up strain due to the charging within the surface layers. (For interpretation of the references to colour in this figure legend, the reader is referred to the web version of this article.)

temperature stabilized to 0.1 °C and the buffer solutions are injected with the following volumes and speeds to enable quick mixing and pH change. First a volume of 400 ul is injected with 100 ul/min and then again 400 ul of the same solution is flown gently with a speed of 20 ul/min across the sensing array to maintain the conditions for 20 min before the pH is changed to a different value.

As reported in Fig. 6, the leading effect on frequency variations during pH change is due to the deprotonation of the silanol groups in the natively oxidized silicon structure (Si_x/SiOH) [23,25,26] at pH higher than 8.5. The built up negative charges tune the stiffness and therefore the frequency of the cantilevers within the array. This has also been observed in stress-induced frequency changes in piezo–electric single clamped beams in vacuum [27]. Building up a highly repulsive charge configuration along the upper and lower surface during pH variations affects sensor stiffness (surface elasticity) and follows a surface-layer model [28] (see Supplementary information).

As can be noticed in Fig. 6 (a), a Δ in frequency of ~800 Hz (~0.13%) is recorded when a switch between pH 2.5 and pH 11 happens on blank silicon sensor arrays (shown in Fig. 5) due to deprotonation and negative charging of the silicon sensors. This sensor array was not coated with Ti/Au and exposes the native silicon oxide to the solutions. During the pH switch of the consecutively injected solutions no molecules are binding covalently to the silicon inteface but the resonance frequency at the higher mode $f_{r,n}$ is changing. As reported the physical dimensions of the sensors are in the micrometer regime (L 400 µm, W 70 µm, T 2.3 µm). In liquid, the motion of the cantilever experiences damping, because not only the cantilever, but also a specific amount of the surrounding fluid is displaced. This additional mass m_l, or virtual mass, is proportional to the displaced mass of the fluid. While vibrating at a higher resonant modes (i.e. 6th mode in these measurement) throughout the whole

experiments, a constant co-moved liquid m_l is accelerated [29]. Therefore the total mass m_{tot}, mass of the cantilever m_c and the co-moved liquid m_l remains constant during the pH switch from pH 2.5 to pH 11. The change in pH does not change the density nor the viscosity of the fluid. The only parameter available for physical change remains the spring constant k of the sensors. This provides a direct correlation from the frequency $f_{r,n}$ to the spring constant k, see eq. 5 in Supplementary information. An increase/decrease of spring constant during theses solution cycles indicates a change in surface strain of the sensors. This is the reflected in an increase in the relative spring constant (right axis of the plot) in the phase where the sensors are exposed to high pH solution pH 11. The derivation of the changes in spring constant can be followed in the Supplementary information.

The charge-derived effect on natively oxidized silicon surfaces Fig. 6 (a) is consistent in the experiments of the SAM-functionalized cantilever array exposed to variable pH conditions presented in Fig. 6 (c). The chemical end-group of the SAM presented to the surrounding liquid environment plays a role in creating an additional trend of frequency shifts (Δ). Water, hydroxy ions and protons can freely penetrate and migrate through the self-assebled monolayers to the underlying hydrophilic subtrate [30]. This is corroborated by the observation that the chemical functional SAMs (-OH, -NH_2, -COOH) alter the SAM packing arrangements and a more disordered SAM surface structure is presented in aqueous environments [31,32]. The thin polycrystalline gold layers provide an optically thight reflective surface for sensor readout. There can be additional pinholes and gaps in the poly crystalline Au/Ti coated interface where further interactions of the hydroxy ions and protons can cause a local effect on the silanol groups of the underlying silicon sensor interface. Referring to Fig. 6 (c), the presence of negative charges derived by the complete deprotonation of the carboxylic acid (11-Mercaptoundecanoic acid funcionalized Cls) leads from a fully relaxed sensor at pH 2.5 to a change in the surface stress along the cantilever after injection of a pH 11 solution. This can be seen in a minor extent on the amine-presenting cantilevers (11-Amino-1-undecanethiol-functionalized CLs). At pH 2.5 the NH_2 sensors exhibit a positive charge in the solution exposed SAM functional group due to the full protonation to NH_3^+ which leads to a slight strain in the sensor surface compared to the other functionalized sensors. The hydroxy-exposing sensors (Hydroxy-1-undecanethiol) exhibit a frequency shift during the pH changes, their frequency behaviour comparable to and dominated by the underlying silicon sensor surface. At pH 11,100% of the carboxylic endgroups (-COO^-) are deprotonated and negatively charged. Toghether with the negative charge of the underlying silanol groups this results in a maximal strain of the sensors. Approximaletly 20% of the NH_3^+ are still positivley charged at pH 11, the remaining groups turned neutral NH_2 providing a lower maximum frequency compared to COO^- sensors.

A hydrophobic effect leads the response of the 1-undecanethiol (-CH_3), in aqueous solutions with the generation of an increased surface stress due to the repulsion of the exposed groups to the liquid environement. The quality of the packing of the -CH_3 monolayers is much better than the three other SAMs. The surface groups can be atomically resolved and show a quasi crystalling packing. Nevertheless the SAM-CH_3 films show 'grain' boundaries within the layer. The spacing of the individual molecular groups is ~21 $Å^2$, larger than the underlying spacing in the gold structure providing access to water, protons and hydroxyl ions [22,33]. The 'confinement' of the underlying negative charges below the hydrophobic SAM layer in the silicon interface at high pH seems to amplify the strain built up in these sensors. The strain can be fully released compared again at low pH environments – comparable to blank silicon and SAM-OH.

Referring to Fig. 6 (d), the charges accumulated on the cantilevers' surface influence the strain in the sensors. To elucidate the mechanical changes of the individual sensors, we normalized the starting frequencies at their highest point before the pH is switched with an injection of a citric acid solution at pH 2.5. All of the sensors undergo a softening due to the loss of negative charge and the net sensor electrical charges turn neutral. The SAM-NH_2 is switching to a SAM-NH_3^+. The complete protonation of the amine group presented on the 11-Amino-1-undecanethiol-functionalized Cls at pH 2.5 leads to resonance frequency shift towards slightly higher frequencies compared to the other functionalized sensors. Some residual mechanical strain being fully positively charged remains. The carboxylic acid groups (11-Mercaptoundecanoic acid) exposed COOH-groups lost all their charge (close to 100% at pH 2.5) rendering a charge neutral sensor and therefore lead to a maximum mechanical relaxation of these sensor (a few mN/m). Similar outcome is recorded at low pH for 11-Hydroxy-1-undecanethiol funcionalized Cls (-OH) and 1-undecanethiol (-CH_3). The strain they can release is direclty proportional to the charges generated at the underlying silicon interface (see discussion above).

5. Conclusions

We successfully fabricated Silicon microcantilevers arrays, with a yield higher than 95%. The best top protection before dry-etch release from the backside, is a multilayer of Al (1um) and Parylene (5um): the Al layer shields the silicon from Parylene residues, while Parylene is conformal and protects the cantilevers sides during the release.

The sensor arrays were tested successfully in a liquid environment. The sensors could individually be functionalized with self-assembled monolayers exposing various end-groups into the solution. As test set hydrophilic (-OH), hydrophobic (-CH_3), acidic (-COOH) or basic (−NH_2) surfaces were introduced and compared to bare silicon interfaces. The modified sensors were oscillated at the 6th normal higher mode in aqueous solutions of different pH (2.5, 11). The chemical end-groups (self-assembled monolayers and native oxide silanols) exposed to high pH 11 induced negative charges due to deprotonation in silanols and carboxy-groups. The thin polycrystalline Ti/Au sensor coating is optically tight for laser reflection but leaves pinholes and crevices that provide access to hydroxyl ions and protons for chemical action in the underlying native silicon oxide. This leads to deprotonation at high pH and the negative charges induced strain is proportional to the quantity and confinement of charges at the interface [28]. These built-up strains could be fully relaxed when exposed again to low pH environments. Amine self-assembled monolayers surfaces built up some strain due to positive charges under low pH conditions resulting in a slightly higher resonance frequency compared to the other three surface chemical functionalities.

These sensor arrays were previously successfully tested in biodiagnostic experiments. A differential analysis (see also fig. S3b) that chooses an in-situ reference sensor in real-time achieves the ultimate sensitivity [4]. Discrimination of quantitative molecular differences of a single amino acid within the binding receptor domain in a diagnostic target was demonstrated. Critical in such assays is that the pH in the surrounding solution during the experimental run is kept constant at physiological levels and that the internal reference control sensors are coated with a receptor with comparable chemical composition that cannot recognize the target entity.

CRediT authorship contribution statement

G. Brunetti: Validation, Formal analysis, Data curation, Visualization, Writing – original draft, Writing – review & editing. **A. De Pastina:** Methodology, Validation, Investigation, Writing – original draft, Writing – review & editing. **C. Rotella:** Investigation. **V. Usov:** Methodology, Investigation. **G. Villanueva:** Writing – review & editing, Funding acquisition. **M. Hegner:** Conceptualization, Validation, Formal analysis, Investigation, Writing – original draft, Writing – review & editing, Funding acquisition, Supervision.

Declaration of competing interest

The authors declare that they have no known competing financial interests or personal relationships that could have appeared to influence the work reported in this paper.

Data availability

Data will be made available on request.

Acknowledgements

The authors would like to thank for funding of the projects SFI/15/IA/3023 Science Foundation Ireland and project 200020_184935 and CRSII5_189967 by the Swiss National Science Foundation (SNF). We thank the NEMS Lab team's members and the CMi at EPFL for their fruitful discussions and their continuous support.

Appendix A. Supplementary data

Supplementary data to this article can be found online at https://doi.org/10.1016/j.mee.2024.112154.

References

[1] G. Binnig, C.F. Quate, C. Gerber, Atomic force microscope, Phys. Rev. Lett. 56 (9) (1986) 930.
[2] G. Brunetti, A. De Pastina, M. Hegner, Rapid label-free nanotechnological immunoassay for analysis of candidate malaria vaccines, Appl. Cell Biol. 9 (2) (2021) 29–32.
[3] G. Brunetti, F. Padovani, A. De Pastina, C. Rotella, A. Monahan, S.L. Hoffman, S. A. Jongo, S. Abdulla, G. Corradin, G. Pluschke, C. Daubenberger, M. Hegner, Nanotechnological immunoassay for rapid label-free analysis of candidate malaria vaccines, Nanoscale 13 (4) (2021) 2338–2349.
[4] G. Brunetti, A. De Pastina, M. Hegner, Quantitative epitope analysis reveals drastic 63% reduced immuno-affinity and 60% enhanced transmissibility for SARS-CoV-2 variants, Nanoscale Adv. 3 (2021) 6903–6911.
[5] J. Zhang, H.P. Lang, F. Huber, A. Bietsch, W. Grange, U. Certa, R. McKendry, H.-J. Güntherodt, M. Hegner, C. Gerber, Rapid and label-free nanomechanical detection of biomarker transcripts in human RNA, Nat. Nanotechnol. 1 (3) (2006) 214.
[6] F. Padovani, J. Duffy, M. Hegner, Microrheological coagulation assay exploiting micromechanical resonators, Anal. Chem. 89 (1) (2016) 751–758.
[7] N. Maloney, G. Lukacs, J. Jensen, M. Hegner, Nanomechanical sensors for single microbial cell growth monitoring, Nanoscale 6 (14) (2014) 8242–8249.
[8] T. Braun, M.K. Ghatkesar, N. Backmann, W. Grange, P. Boulanger, L. Letellier, H.-P. Lang, A. Bietsch, C. Gerber, M. Hegner, Quantitative time-resolved measurement of membrane protein–ligand interactions using microcantilever array sensors, Nat. Nanotechnol. 4 (3) (2009) 179–185.
[9] A. Martín-Pérez, D. Ramos, Nanomechanical hydrodynamic force sensing using suspended microfluidic channels, Microsyst. Nanoeng. 9 (1) (2023) 53.
[10] T.P. Burg, M. Godin, S.M. Knudsen, W. Shen, G. Carlson, J.S. Foster, K. Babcock, S. R. Manalis, Weighing of biomolecules, single cells and single nanoparticles in fluid, Nature 446 (7139) (2007) 1066–1069.
[11] A. De Pastina, PZE-Transduced Suspended Microchannel Resonators for Sensing Applications, Lausanne, EPFL, Swiss Federal Institute of Technology Lausanne, 2018, p. 179.
[12] S. Bianco, M. Cocuzza, S. Ferrero, E. Giuri, G. Piacenza, C.F. Pirri, A. Ricci, L. Scaltrito, D. Bich, A. Merialdo, P. Schina, R. Correale, Silicon resonant microcantilevers for absolute pressure measurement, J. Vacuum Sci. Technol. B: Microelect. Nanometer Struct. 24 (2006) 1803–1809.
[13] A. Greve, J. Olsen, N. Privorotskaya, L. Senesac, T. Thundat, W.P. King, A. Boisen, Micro-calorimetric sensor for vapor phase explosive detection with optimized heat profile, Microelectron. Eng. 87 (5) (2010) 696–698.
[14] J. Barnes, R. Stephenson, C. Woodburn, S. Oshea, M. Welland, T. Rayment, J. Gimzewski, C. Gerber, A femtojoule calorimeter using micromechanical sensors, Rev. Sci. Instrum. 65 (1995) 3793–3798.
[15] H.P. Lang, M. Hegner, C. Gerber, Nanomechanical cantilever array sensors, in: B. Bhushan (Ed.), Springer Handbook of Nanotechnology, Springer Berlin Heidelberg, Berlin, Heidelberg, 2010, pp. 427–452.
[16] A. Boisen, S. Dohn, S.S. Keller, S. Schmid, M. Tenje, Cantilever-like micromechanical sensors, Rep. Prog. Phys. 74 (3) (2011) 036101.
[17] A. De Pastina, F. Padovani, G. Brunetti, C. Rotella, F. Niosi, V. Usov, M. Hegner, Multimodal real-time frequency tracking of cantilever arrays in liquid environment for biodetection: comprehensive setup and performance analysis, Rev. Sci. Instrum. 92 (6) (2021).
[18] M. Walther, P.M. Fleming, F. Padovani, M. Hegner, An optimized measurement chamber for cantilever array measurements in liquid incorporating an automated sample handling system, EPJ Tech. Instrum. 2 (1) (2015) 7.
[19] G. Brunetti, Nanotechnological Cantilever-Based Analysis of Infectious Disease Biomarkers, School of Physics, Trinity College Dublin, Dublin, TCD, 2022.
[20] H. Seidel, L. Csepregi, A. Heuberger, H. Baumgärtel, Anisotropic etching of crystalline silicon in alkaline solutions: I. Orientation dependence and behavior of passivation layers, J. Electrochem. Soc. 137 (11) (1990) 3612.
[21] M.J. Madou, Fundamentals of Microfabrication and Nanotechnology, 3rd ed., CRC Press, Boca Raton, 2011.
[22] A. Ulman, Formation and structure of self-assembled monolayers, Chem. Rev. 96 (4) (1996) 1533–1554.
[23] M. Sulpizi, M.-P. Gaigeot, M. Sprik, The silica–water interface: how the silanols determine the surface acidity and modulate the water properties, J. Chem. Theory Comput. 8 (3) (2012) 1037–1047.
[24] G. Gonella, E.H.G. Backus, Y. Nagata, D.J. Bonthuis, P. Loche, A. Schlaich, R. R. Netz, A. Kühnle, I.T. McCrum, M.T.M. Koper, M. Wolf, B. Winter, G. Meijer, R. K. Campen, M. Bonn, Water at charged interfaces, Nat. Rev. Chem. 5 (7) (2021) 466–485.
[25] M. Morita, T. Ohmi, E. Hasegawa, M. Kawakami, M. Ohwada, Growth of native oxide on a silicon surface, J. Appl. Phys. 68 (3) (1990) 1272–1281.
[26] L. Chen, D. Ngo, J. Luo, Y. Gong, C. Xiao, X. He, B. Yu, L. Qian, S.H. Kim, Dependence of water adsorption on the surface structure of silicon wafers aged under different environmental conditions, Phys. Chem. Chem. Phys. 21 (47) (2019) 26041–26048.
[27] R.B. Karabalin, L.G. Villanueva, M.H. Matheny, J.E. Sader, M.L. Roukes, Stress-induced variations in the stiffness of micro- and nanocantilever beams, Phys. Rev. Lett. 108 (23) (2012) 236101.
[28] G.-F. Wang, X.-Q. Feng, Effects of surface elasticity and residual surface tension on the natural frequency of microbeams, Appl. Phys. Lett. 90 (23) (2007) 231904.
[29] T. Braun, V. Barwich, M.K. Ghatkesar, A.H. Bredekamp, C. Gerber, M. Hegner, H. P. Lang, Micromechanical mass sensors for biomolecular detection in a physiological environment, Phys. Rev. E 72 (3) (2005) 031907.
[30] J.M.D. Lane, M. Chandross, C.D. Lorenz, M.J. Stevens, G.S. Grest, Water penetration of damaged self-assembled monolayers, Langmuir: ACS J. Surf. Colloids 24 (11) (2008) 5734–5739.
[31] P. Wagner, M. Hegner, P. Kernen, F. Zaugg, G. Semenza, Covalent immobilization of native biomolecules onto Au (111) via N-hydroxysuccinimide ester functionalized self-assembled monolayers for scanning probe microscopy, Biophys. J. 70 (5) (1996) 2052–2066.
[32] G.E. Poirier, E.D. Pylant, J.M. White, Crystalline structures of pristine and hydrated mercaptohexanol self-assembled monolayers on Au(111), J. Chem. Phys. 104 (18) (1996) 7325–7328.
[33] L.H. Dubois, B.R. Zegarski, R.G. Nuzzo, Molecular ordering of organosulfur compounds on Au(111) and Au(100): adsorption from solution and in ultrahigh vacuum, J. Chem. Phys. 98 (1) (1993) 678–688.

Silicon Microresonator Arrays: A comprehensive study on Fabrication Techniques and pH-controlled stress-induced variations in cantilever stiffness

G. Brunetti [a, b, c], A. De Pastina [d], C. Rotella [c] V. Usov [c], G. Villanueva [e] and M. Hegner [c*]

[a] Tissue Engineering Research Group (TERG), Department of Anatomy & Regenerative Medicine, Royal College of Surgeons in Ireland (RCSI), Dublin, Ireland
[b] Advanced Materials and BioEngineering Research (AMBER) Centre, Trinity College Dublin (TCD), Dublin, Ireland
[c] Center for Research on Adaptive Nanostructures and Nanodevices (CRANN), School of Physics, Trinity College Dublin (TCD), Dublin, Ireland
[d] Silicon Austria Labs, Sensor System, Microsystem Technologies, Villach, Austria
[e] Swiss Federal Institute of Technology Lausanne (EPFL), Switzerland

*Corresponding author: hegnerm@tcd.ie

Supplementary information

Evaluation of sensor geometries for subsequent microfabrication batch processing

Postprocessing of 8-microcantilever silicon chip devices

Test versions of cantilevers of different geometry were produced prior to the wafer-scale design and fabrication. The width of the cantilevers was reduced as compared to the previous benchmarking 8-cantilever Si microchip devices, in order to place a higher number of cantilevers on every chip (500×100×0.5 up to 500×100×7 μm) [1-4]. The higher number of sensors allow for better statistics in experimental assessments of similarly functionalized individual sensor groups and allow for more individual parallel targets in diagnostic applications. Other dimensions of the cantilevers were adjusted according to requirements of the resonant frequency. The position sensitive laser detector of the platform exhibits an upper limit of 5 MHz and the internal piezo actuation of the sensors levels off at ~2 MHz. Ideally, we target up to 12 resonant peaks in liquids within the frequency domain up to 2 MHz. For that, the cantilevers on the 8-cantilever devices were modified by two methods both using a dual column Focused Ion Beam (FIB) system (Zeiss Auriga) at 30 keV beam energy and 10 nA beam current.

In the first method, 7 μm thick cantilevers on an 8-cantilever microchip were first reduced in thickness by etching them in the mixed SF_6 and CHF_3 inductively coupled plasma (ICP) using an Oxford Instruments Plasmalab etching tool (SF_6 and CHF_3 flow rates 33 and 50 sccm respectively, 1200 W AC Power, 10 V DC bias). Then cantilevers of smaller lateral dimensions were directly cut out of larger cantilevers by the FIB milling (Fig. S1(a)).

In the second method, dimensions of the 500×100 μm cantilevers were changed by the four-step process combining the direct-wright FIB lithography and ICP etching. Cantilevers on the 8-cantilever microchips were first reduced to a desired thickness by etching them in the CHF_3-SF_6 ICP. Then a rectangular pattern of Ga ions was implanted into the cantilever top surface by a low-dose non-milling FIB at a dose level of the order of 10^{17} ions/cm^2. Ga penetrated into the first few nanometers of Si surface and created a hard mask resistant to the plasma etching (Fig. S1(b)). The unmasked Si was anisotropically etched at a rate 12.5 nm/s in the SF_6-CHF_3 ICP and the mask was removed by short etching in the sulfur hexafluoride plasma. Thus cantilevers of the same thickness but different lateral dimensions could be created on the same chip including pairs of cantilevers hanging on the same hinge (Fig. S1(c)). However, not all the cantilevers produced by this method were not suitable as a prototype by the end of the process. First, cantilevers bent downwards under the strain created by

implantation in the top surface and then upwards after the mask was removed and the strain was released ((Fig. S1(d)).

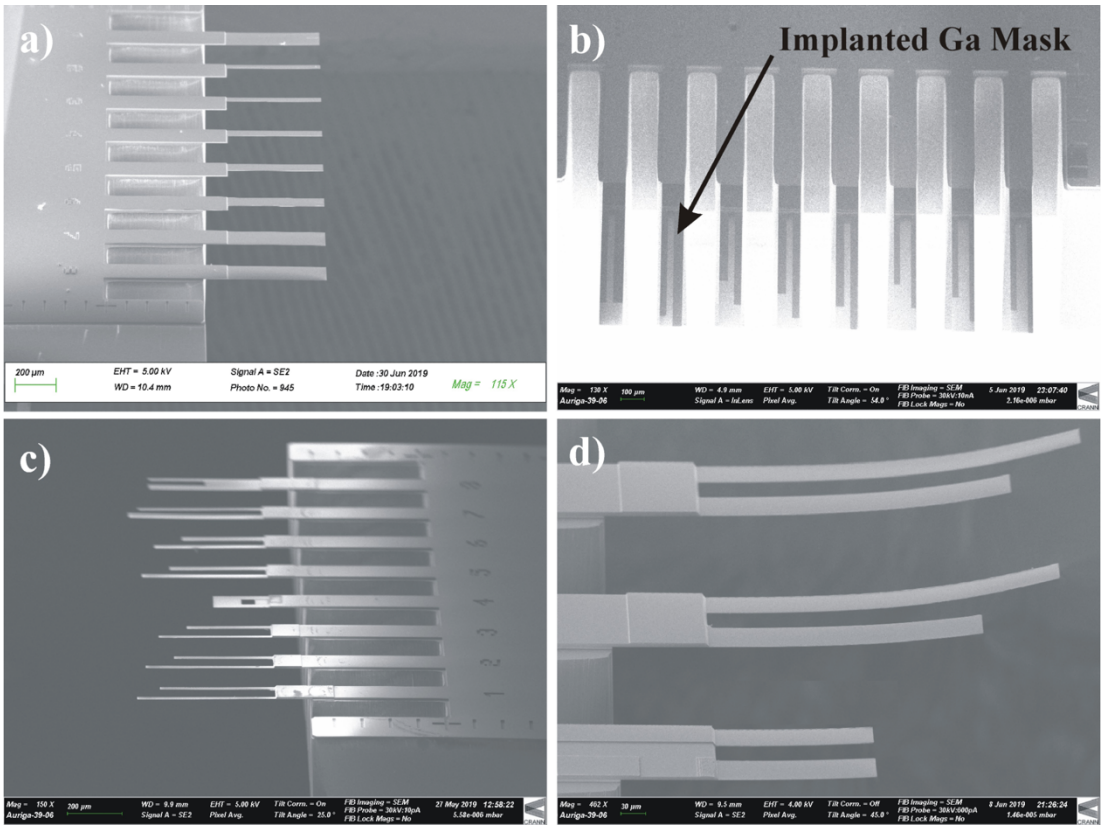

Figure S1. Test cantilever fabrication (a) SEM image of a microchip where the size of cantilevers # 2 - 6 was reduced directly by FIB milling; the modified cantilevers' width varies from 25 to 60 µm respectively (b) SEM image of an 8-cantilever microchip with a Ga etching mask on top of the cantilevers; (c) SEM image of an 8-cantilever microchip after the ICP etching; Si unprotected by the hard mask has been removed; the base of the cantilever # 4 was used for the FIB Write Field alignment prior to the implantation therefore most of the cantilever has been removed by the ICP etching (d) SEM image of cantilevers bent upwards after the Ga mask removal; first, cantilevers bent downwards under the strain created by implantation and then upwards after the mask was removed.

Resonance frequencies analysis of FIB milled dual and single cantilevers

Resonant properties of the test cantilevers were analyzed in liquid environment using the home-built nano-mechanical platform for label-free detection of target biomolecules [5]. A set of cantilever chips where the thickness of the sensors was reduced down to 2.5 µm was further processed by FIB to receive dual sensors on individual sensors with the following geometries as shown in Table S1.

Table S1: Cantilever geometries after FIB milling

Cantilever position	**Length [µm]**	**Width [µm]**	**Thickness [µm]**
CL 1	500	100	2.5
CL 2a	500	22	2.5
CL 2b	283	25	2.5
CL 3a	500	25	2.5
CL 3b	400	29	2.5
CL 4a	500	30	2.5
CL 4b	297	27	2.5
CL 5a	500	31	2.5
CL 5b	300	40	2.5
CL 6	500	100	2.5

The sensors were oscillated in nanopure water by external piezo actuation [6]. For comparison the non-modified cantilever sensor in position CL1 was also frequency analyzed (see figure S2 blue dashed line). A regular sensor with the original geometry (length 500 µm, width 100 µm and thickness 2.5 µm) will have its theoretically calculated resonance modes at the following frequencies shown in table S2. The measured resonances in liquids were found to be within $\pm$ 10% of these values.

Table S2: Calculated cantilever longitudinal resonances in water at 23 °C utilizing a Young's modulus for silicon of 169 GPa. [7]

	Mode 1 [kHz]	Mode 2 [kHz]	Mode 3 [kHz]	Mode 4 [kHz]	Mode 5 [kHz]	Mode 6 [kHz]	Mode 7 [kHz]	Mode 8 [kHz]	Mode 9 [kHz]	Mode 10 [kHz]
Calculated	3.27	21.38	63.64	132.84	232.55	366.32	536.79	746.32	996.98	1290.56
Measured			68.75	141.25	231.25	338.75	485.0	678.75	917.5	

First we analyzed the FIB milled double cantilever pairs cut from one 500x100 µm cantilevers as shown in figure S2a,b). After milling the most indicative analysis for subsequent quantitative diagnostic sensing performance of the four sets of cantilevers the is the frequency behavior in a liquid environment. Upon immersion into liquid environment resonance modal frequencies of the cantilever sensors are reduced globally due to the denser media they are oscillating in, and their oscillation quality is damped due to the liquid drag that is dissipating energy. For a mathematical analysis of cantilever sensors immersed in a viscous medium please see refs. [7-10]

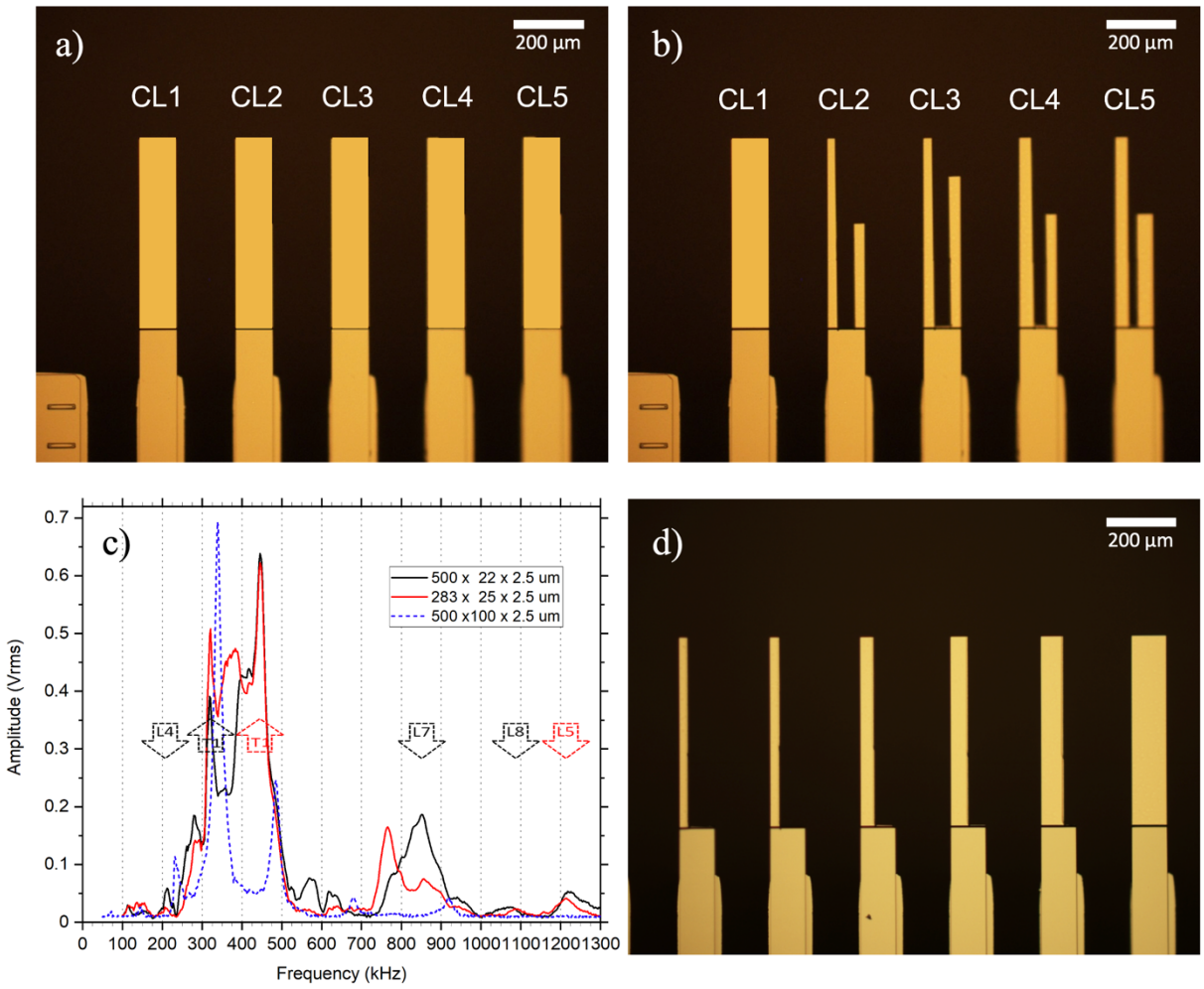

Figure S2. Test cantilever fabrication (a) SEM image of a microchip before FIB milling (b) SEM image of a microchip after FIB milling where the size of cantilevers # 2 - 5 was machined to receive two adjacent modified cantilevers' with width varies from 22 to 40 µm from within an original cantilever respectively (c) Oscillation frequency analysis in liquid of CL1 and each individual FIB machined cantilever sensor from CL2 (see 2b) (arrow down describes regions of mechanical cross-talk of a longitudinal oscillation mode, arrow up a torsional oscillation mode of the respective sensor;

(d) SEM image of 6 individual sensors cantilevers in position 2-6 from a 8-sensor microchip after FIB (see 1a). Original cantilever sensor dimensions before machining FIB 500 x 100 x 2,5 µm, after FIB milling a length of 500 µm with a width of 22, 26, 40, 50, 63 µm respectively. The asymmetric clamping point of such sensors shows a tendency to induce torsional oscillation modes.

As shown in the vibrational analysis in liquid (Fig. S2c) the narrower and shorter cantilever exhibit a distinct oscillation behavior. Two peaks are dominating the frequency spectrum (T1 (black), T1 (red)), these are the first torsional modes of the adjacent sensors [8]. The individual longitudinal modes are easily discerned. The torsional mode of the original 500 x 100 µm sensor (blue dashed) is not visualized since it is located at ~50 kHz. What is clearly shown is, that the sensors CL 2a and CL 2b that are anchored at the same hinge of the chip body are exhibiting some mechanical frequency cross-talk across the structure (indicated in the frequency regions by the respective arrows of the longitudinal and torsional mode of the FIB machined sensor. For instance, at 851,4 kHz – the 7th longitudinal mode of the 500 x 22 µm sensor is transferring its oscillation onto the sensor with smaller dimensions and exciting that sensor with an amplitude of ~40% at the same frequency where no longitudinal mode should be observed. Narrower cantilevers are easier excited in a torsional mode than wider ones. In a further focused ion beam batch the second of the cantilevers on the same hinge structure was omitted ((Fig. S2d). Analyzing the resonance frequency spectra in liquid revealed that the mechanical cross-talk in all sensors disappeared. This led to the conclusion that a way forward to evolve from the 1 x 8 microcantilever sensor arrays was to generate individual microcantilever sensors chips at a higher sensor number across the chip body with reduced width of the crucial comb and hinge structure that mechanically separated the oscillation of the individual sensors.

The final design of the devices consisted of 18-cantilever arrays (400×70×2.3 µm respectively). Such sensors display 10 to 8 resonance frequency modes within the bandwidth of 1.5 MHz. The rather large planar surface area (length x width) enables also to accommodate enough biomass in liquid diagnostic assays, as it was shown that the mechanical noise level in liquids at the moment is around 1 pg bound mass [5]

Derivation of the Spring Constant in a single clamped oscillating beam

The frequency of an oscillating cantilever beam $f_{R,n}$ clamped at one end immersed in a liquid is defined as [7, 10-12]:

$$f_{R,n} = c_n \sqrt{\frac{k}{m_c + \Gamma_r^f(Re_n, \kappa_n) m_l}} \qquad (1)$$

Where k is the spring constant. The parameters m_c and m_l are, respectively, the mass of the cantilever and a "virtual mass" of inviscid liquid co-moved by the cantilever when $\kappa_n = 0$. Both masses are evaluated from the density of the cantilever ρ_c and the density of the liquid ρ_l as $m_c = \rho_c bhl$ and $m_l = \pi\rho_l b^2 l/4$ with b width, h height and l length. The Reynold's number $Re = 2\pi f\rho_l b^2/\eta$ expresses the importance of inertial forces in the liquid relative to viscous forces (η is the viscosity of the liquid). the pre-factors c_n and β_n are correlated to the geometry of the sensors and the oscillation mode number and defined as:

$$c_{n=} \frac{\beta_n^2}{2\pi\sqrt{3}} \qquad (2)$$

$$\beta_n = 1.875, 4.694, 7.854, 11, \ldots, \pi(n - 0.5) \qquad (3)$$

When the frequency changes but the mass does not change then the derivation of the spring constant follows. In our current assay a sensor is subjected to the same density and ionic strength of a liquid throughout, the hydrodynamic function stays the same and also the co-moved liquid mass. The cantilever mass m_c does not change and the term with the hydrodynamic function and the co-moved

mass m_l remains constant when solutions with the same ionic strength and the same density/viscosity are inject. So the term m_{tot} remains constant throughout the experiment.
The resonance frequency under these conditions simplify to the term:

$$f_{r,n} = c_n \sqrt{\frac{k}{m_{tot}}} \qquad (4)$$

with m_{tot} remaining constant during the experimental observations. Then the spring constant can directly be back calculated from the frequency readings as:

$$f_{r,n}^2 \frac{m_{tot}}{c_n^2} = k \qquad (5)$$

$$\text{with } c_n^2 = \frac{\beta_n^4}{12\pi^2} \text{ and } \beta_n^4 = \pi^4 (n - 0.5)^4$$

We can compute how much the spring constant k changes in oscillation mode 6 when we change the pH from the conversion of the change in resonance frequency. The pH switch experiments are repeatable and reproducible, the switching pattern of the frequencies is remaining constant, all the frequencies are increasing when the pH is shifted to values above the pKa of the involved surface functional groups. With regards to the frequency increase self-assembled monolayers with different chemical end groups exposed to the liquid are behaving slightly different. During the pH switch the density and the viscosity of the solution do not change.

Total surface stress generated during the pH change
Due to the order of magnitude of the calculated total surface stress σ_s^T (several tens of N/m) arising during the pH switches [13]

$$\sigma_s^T \approx \frac{\Delta\omega}{0.042\ \omega_0} \frac{Eh}{\nu(1-\nu)} \left(\frac{l}{b}\right) \left(\frac{h}{b}\right)^2 \qquad (6)$$

with ω as angular resonant frequency ($\omega = 2\pi f$), ν, the Poisson's ratio (0.49) and E, the Young's modulus, the frequency observations measured during pH change most probably do not represent only strain-independent surface stress [13]. Gurtin et al. [14, 15] concluded that surface elasticity influences the natural frequency of microbeams but residual surface stress does not. They postulate that the surface obeys a stress-strain relation of the form

$$\sigma_s^T = \sigma + \kappa\epsilon \qquad (7)$$

where σ_s^T is the total surface stress, σ is the surface stress in the pre-stressed configuration before vibration, ϵ is the strain measured from the pre-stressed configuration, and κ is the surface elasticity. In our measurements the surface elasticity would change due to charging at the two sensor interfaces (building up highly repulsive charge configuration along the upper and lower surface), this would be based on a surface-layer model [16]. These changes directly affect the stiffness of the single clamped cantilever sensors.

Charges per sensor
According to literature a single hetero-bifunctional aliphatic thiol occupies 21.4Å^2 per molecule [17, 18]. The sensor dimensions in the used arrays are 70000 nm x 400000 nm x 2300 nm, and their volume is 6.44 x 10^{13} nm^3. The surface area per sensor is: 2 x 70000 nm x 400000 nm = 5.6 x 10^{10} nm^2 plus two side walls 2 x 400000 nm x 2300 nm = 1.84 x 10^9 nm^2 plus one front face 70000 nm x 2300 nm = 1.61 x 10^8 nm^2, resulting in a total of = 5.8 x 10^{10} nm^2. With 4.673 thiol SAM molecules per nm^2 a maximum 2.71 x 10^{11} thiols and functional groups per sensor can theoretically be accommodated.

Switching from pH 2.5 to pH 11 (Fig. S3a), the OH-SAM frequency is increasing the least and follows the changes of a SiO_x/OH sensor array that has not been coated at all. The native SiO_x/OH surface exposes silanol groups that deprotonate at pH above 8.5 [19]. Analyzing the frequency increases the SAM-NH_3^+ and the SAM-CH_3 follow. The most frequency increase is experienced on SAM-COOH. The pKa of SAM-COOH is around pH 4,5 so at pH 2.5 pH it is charged at a ratio of 1:100 (COO^-:COOH). The $NH_3^+ : NH_2$ has a ratio of 10'000'000:1 at pH 2.5 with a pKa at 10.5. When the pH is raised to 11 the ratios are changing inversely. The SAM-COOH gets fully deprotonated to COO^- with a ratio of 5'000'000:1 (COO^-:COOH) and the SAM-NH_2 loses its positive charge to have a ratio of 1:5 ($NH_3^+ : NH_2$).

A jump from pH 2,5 to pH 11 represents a change of 8-orders of magnitude. If 2.71 x 10^{11} COOH groups per sensor are able to be deprotonated to COO^- at pH 11 then having a pKa of 4.5 (SAM-COOH) roughly results in a ratio of 5'000'000:1 groups that are negatively charged (-) i.e. 2.709 x 10^{11} groups and 5.464 x 10^4 are still protonated (neutral).

A differential readout analysis of the sensor responses is allowing to eliminate all the environmental disturbances [20], achieving ultimate resolution at the biological level of the difference of two individual amino acids in receptors on two sensors. The differential analysis in figure S3b), where the sensors functionalized with SAM-OH are taken as internal reference sensors, is highlighting the frequency changes based on the charge/hydrophobicity differences only. Only sensor responses within one array measured simultaneously can be subtracted from each other. The evaluated change upon pH switching of ~1000 Hz in the sensors, corresponds to a mechanical stiffening of the sensors by ~5 mN/m which is a considerable order of magnitude in the field of cantilever sensing and is comparable to the stress induced by hybridization of complementary DNA strands on cantilever sensors [21]. In figure S3c) a timeline of consecutive pH changes for the group of 6 COOH-functionalized is shown. The frequency changes are repeatable and similar in magnitude.

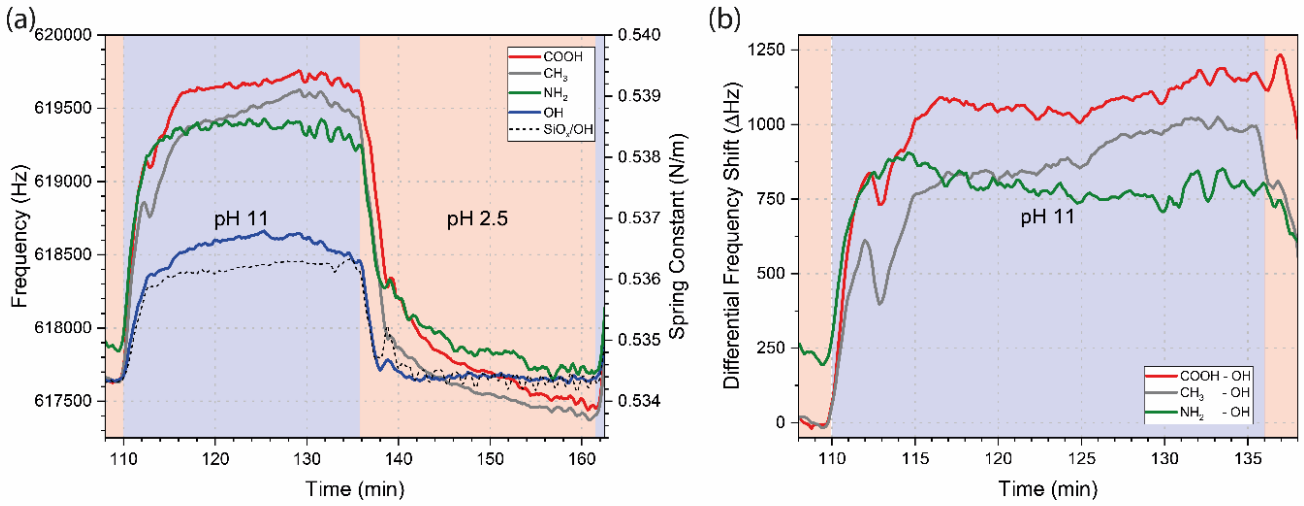

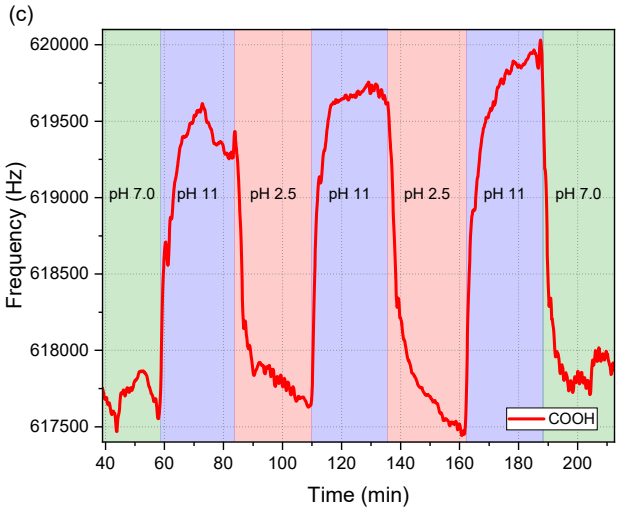

Figure S3. Cantilever array responses to pH changes. (a) SAM functionalized sensors incubated in alternated pH 2.5 – pH 11 – pH 2.5 solutions. SAM-COOH (n=6, red), SAM-NH2 (n=4, green), SAM-OH (n=4, blue), SAM-CH3 (n=4, grey), SiOx/OH (from Figure (6a) as underlying graph, black dashed). At t=110 min the pH is switched from pH 2.5 to 11 and sensor frequency is changing to a higher frequency. After switching back to pH 2.5 at 136 min sensor frequencies recover to a lower value. (b) Differential readout of the sensors during switch to pH 11, as internal reference sensor SAM-OH is chosen. A differential readout confirms the mechanical difference arising due to the different functionalized end groups. (c) Automated consecutive pH changes in the fluidic system starting from a pH 7 and then cycling from pH 2.5 to pH 11 until sensors are again equilibrated at pH7. The frequencies at pH 7 are slightly higher than the ones at pH 2.5 since the protonation of the COO^- end-groups that eliminates charges, is more complete at pH 2.5 for the COOH sensors.

In table S3 representative numerical values for the mechanical changes are indicated.

Table S3: Representative frequency changes by switching solutions from citric acid pH 2.5 to sodium hydroxyde pH 11 and back (see figure S3) on the sensors coated with the respective surface funcitional groups. Evaluated from the value just before the jump till the ~midpoint of the following equilibrium trace.

Frequency change @ pH 11

acid/base	SiO_x/OH	Δ	SAM-OH	Δ	$SAM-NH_2$	Δ	$SAM-CH_3$	Δ	SAM-COOH	Δ
	Hz	Hz	Hz	Hz	Hz	Hz	Hz	Hz	Hz	Hz
pH 2.5	617650	774 (0.12%)	617641	977 (0.16%)	617645	1558 (0.25%)	617645	1859 (0.3%)	617641	2045 (0.33%)
pH 11	618424		618618		619203		619504		619686	

Frequency change @ pH 2.5

acid/base	SiO_x/OH	Δ	SAM-OH	Δ	$SAM-NH_2$	Δ	$SAM-CH_3$	Δ	SAM-COOH	Δ
	Hz	Hz	Hz	Hz	Hz	Hz	Hz	Hz	Hz	Hz
pH 11	618465	821 (0.13%)	618641	975 (0.16%)	619244	1411 (0.23%)	619442	1934 (0.31%)	619618	2019 (0.32%)
pH 2.5	617644		617666		617833		617508		617599	

References:

[1] J. Duffy, F. Padovani, G. Brunetti, P. Noy, U. Certa, M. Hegner, Towards personalised rapid label free miRNA detection for cancer and liver injury diagnostics in cell lysates and blood based samples, Nanoscale 10 (2018) 12797-12804.
[2] T. Braun, M.K. Ghatkesar, N. Backmann, W. Grange, P. Boulanger, L. Letellier, H.-P. Lang, A. Bietsch, C. Gerber, M. Hegner, Quantitative time-resolved measurement of membrane protein–ligand interactions using microcantilever array sensors, Nat. Nanotechnol. 4(3) (2009) 179-185.
[3] A. Bietsch, J. Zhang, M. Hegner, H.P. Lang, C. Gerber, Rapid Functionalization of Cantilever Array Sensors by Inkjet Printing, Nanotechnology 15(8) (2004) 873.
[4] M. Jensen J. and Hegner, Predictions of the Compressible Fluid Model and its Comparison to Experimental Measurements of Q Factors and Flexural Resonance Frequencies for Microcantilevers, Journal of Sensor 2012 (2012) 258381.
[5] A. De Pastina, F. Padovani, G. Brunetti, C. Rotella, F. Niosi, V. Usov, M. Hegner, Multimodal real-time frequency tracking of cantilever arrays in liquid environment for biodetection: comprehensive setup and performance analysis, Rev. Sci. Instrum. 92(6) (2021).

[6] M. Walther, P.M. Fleming, F. Padovani, M. Hegner, An optimized measurement chamber for cantilever array measurements in liquid incorporating an automated sample handling system, EPJ Tech. Instrum. 2(1) (2015) 7.
[7] C.A. Van Eysden, J.E. Sader, Frequency response of cantilever beams immersed in compressible fluids with applications to the atomic force microscope, J. Appl. Phys. 106(9) (2009) 094904.
[8] C.P. Green, J.E. Sader, Torsional frequency response of cantilever beams immersed in viscous fluids with applications to the atomic force microscope, J. Appl. Phys. 92(10) (2002) 6262-6274.
[9] M.K. Ghatkesar, T. Braun, V. Barwich, J.-P. Ramseyer, C. Gerber, M. Hegner, H.P. Lang, Resonating modes of vibrating microcantilevers in liquid, Appl. Phys. Lett. 92(4) (2008) 043106.
[10] T. Braun, V. Barwich, M.K. Ghatkesar, A.H. Bredekamp, C. Gerber, M. Hegner, H.P. Lang, Micromechanical mass sensors for biomolecular detection in a physiological environment, Phys. Rev. E. 72(3) (2005) 031907.
[11] F. Padovani, J. Duffy, M. Hegner, Nanomechanical clinical coagulation diagnostics and monitoring of therapies, Nanoscale 9(45) (2017) 17939-17947.
[12] F. Padovani, J. Duffy, M. Hegner, Microrheological Coagulation Assay Exploiting Micromechanical Resonators, Anal. Chem. 89(1) (2016) 751-758.
[13] M. Lachut, J.E. Sader, Effect of surface stress on the stiffness of cantilever plates, Phys. Rev. Lett. 99 20 (2007) 206102.
[14] M.E. Gurtin, J. Weissmüller, F. Larché, A general theory of curved deformable interfaces in solids at equilibrium, Philosophical Magazine A 78(5) (1998) 1093-1109.
[15] M.E. Gurtin, A.I. Murdoch, Surface Stress in Solids, Int. J. Solids and Structures 14(6) (1978) 431-440.
[16] G.-F. Wang, X.-Q. Feng, Effects of surface elasticity and residual surface tension on the natural frequency of microbeams, Appl. Phys. Lett. 90(23) (2007) 231904.
[17] A. Ulman, Formation and Structure of Self-Assembled Monolayers, Chem. Rev. 96(4) (1996) 1533-1554.
[18] L.H. Dubois, B.R. Zegarski, R.G. Nuzzo, Molecular ordering of organosulfur compounds on Au(111) and Au(100): Adsorption from solution and in ultrahigh vacuum, The Journal of Chemical Physics 98(1) (1993) 678-688.
[19] M. Sulpizi, M.-P. Gaigeot, M. Sprik, The Silica–Water Interface: How the Silanols Determine the Surface Acidity and Modulate the Water Properties, Journal of Chemical Theory and Computation 8(3) (2012) 1037-1047.
[20] G. Brunetti, A. De Pastina, M. Hegner, Quantitative epitope analysis reveals drastic 63% reduced immuno-affinity and 60% enhanced transmissibility for SARS-CoV-2 variants, Nanoscale Advances 3 (2021) 6903–6911.
[21] J. Zhang, H.P. Lang, F. Huber, A. Bietsch, W. Grange, U. Certa, R. McKendry, H.-J. Güntherodt, M. Hegner, C. Gerber, Rapid and label-free nanomechanical detection of biomarker transcripts in human RNA, Nat. Nanotechnol. 1(3) (2006) 214.